Catalysis Science & Technology

ROYAL SOCIETY OF CHEMISTRY

PAPER

View Article Online
View Journal

Cite this: DOI: 10.1039/d6cy00086j

Boosting ammonia decomposition for hydrogen production over Co/CeO_2 catalysts *via* Sr doping

Linghui Su,[a] Fanke Zeng,[a] Jiajie Wang,[b] Qasim Qasim,[a] Xiaoli Liu,[c] Jing Li,[d] Hao Li *[e] and Wanglai Cen*[a]

Received 26th January 2026,
Accepted 26th February 2026

DOI: 10.1039/d6cy00086j

rsc.li/catalysis

The development of efficient and cost-effective catalysts is crucial for ammonia decomposition to establish a carbon-free hydrogen energy system. In this work, we developed a non-noble metal Sr-doped Co/CeO_2 catalyst synthesized *via* a sol–gel method, demonstrating outstanding catalytic performance and stability. It achieved NH_3 conversions of approximately 76% at 500 °C and 95% at 550 °C, maintaining excellent stability over 100 h at a high GHSV of 30 000 mL g^{-1} h^{-1}, which is markedly superior to the undoped Co/CeO_2. Comprehensive characterization reveals that enhanced performance originates from a synergistic promotion mechanism initiated by Sr doping. The dynamic redistribution of incorporated Sr species under reaction conditions is pivotal for maximizing their electron-donating capability. This process concurrently drives the creation of abundant oxygen vacancies and strengthens the metal–support interaction, thereby stabilizing the active cobalt species. These interconnected modifications collectively optimize the electronic structure of the catalyst. The optimized electronic configuration facilitates N–H bond activation while weakening the adsorption of reaction products, ultimately accelerating the overall catalytic cycle. This work underscores that engineering the electronic structure of catalyst supports through aliovalent doping is a highly effective strategy for designing advanced ammonia decomposition catalysts.

Introduction

Hydrogen has emerged as a promising clean energy carrier toward a sustainable and carbon-neutral energy system.[1–3] However, its widespread application is often constrained by challenges related to storage and transportation.[4] Ammonia (NH_3), with its high hydrogen density (17.6 wt%), ease of liquefaction, and well-established infrastructure, is considered to be a promising hydrogen carrier.[4–6] Consequently, catalytic ammonia decomposition has emerged as a key pathway for efficient hydrogen utilization, yet its efficiency critically depends on the development of highly active and stable catalysts.[7] Among various catalytic systems, although ruthenium-based catalysts exhibit superior activity, their high cost and scarcity limit large-scale application.[6,8,9] Consequently, non-noble transition metals such as cobalt (Co) have attracted considerable attention due to their moderate activity, earth abundance, and cost-effectiveness.[10,11] However, the activity and stability of Co-based catalysts require further enhancement to meet practical demands.[1,4]

The performance of Co catalysts is profoundly influenced by their interaction with the support material, which can modulate metal dispersion, electronic structure and stability. Among various supports, ceria (CeO_2) has been extensively investigated as a catalyst support due to its unique redox properties and high oxygen storage capacity, stemming from the facile Ce^{4+}/Ce^{3+} transition and the formation of oxygen vacancies.[12–16] To further unlock the potential of Co/CeO_2 systems for ammonia decomposition, rational modification of the support is essential.

Aliovalent doping with alkaline earth metals has emerged as a powerful approach to tailor the properties of CeO_2-supported non-noble metal catalysts.[17,18] Beyond the well-established role of generating oxygen vacancies for charge compensation, such dopants impart multiple beneficial effects.[18,19] They act as electronic modifiers, directly perturbing the electron density of supported non-noble metal nanoparticles.[20,21] Simultaneously, they can strengthen the metal–support interface to enhance dispersion and inhibit sintering of the active phase.[19,22] Moreover, doping can modulate the surface acid–base properties, thereby optimizing the adsorption strength of reactants and intermediates.[20,23] These combined electronic

[a] *Institute of New Energy and Low-Carbon Technology, Sichuan University, Chengdu 610065, China. E-mail: cenwanglai@scu.edu.cn*
[b] *National Key Laboratory of Porous Materials for Gas Separation and Conversion, Southwest Institute of Chemical Co., Ltd., Chengdu 610225, China*
[c] *Sichuan Shunan Xingzhu Ecological Technology Co., Ltd., Yibin 644000, China*
[d] *College of Carbon Neutrality and Future Technology, Sichuan University, Chengdu 610065, China*
[e] *Advanced Institute for Materials Research (WPI-AIMR), Tohoku University, Sendai, Miyagi 980-8577, Japan. E-mail: li.hao.b8@tohoku.ac.jp*

and structural modifications are particularly advantageous for reactions such as ammonia decomposition. Among alkaline earth dopants, strontium (Sr^{2+}) is particularly promising. Its suitable ionic radius allows for effective incorporation into the ceria lattice, which in turn exerts a pronounced ability to modulate the redox properties and electronic structure of the ceria.[20] Despite these recognized benefits, the specific role of Sr^{2+} doping in tuning the Co/CeO_2 system for ammonia decomposition remains underexplored. A fundamental understanding of how Sr incorporation affects the electronic structure of Co active sites, the metal–support interaction, and ultimately the reaction pathway is crucial for rational catalyst design.

Herein, we report the design and synthesis of a Sr-doped Co/CeO_2 catalyst ($Co/Sr–CeO_2$) that exhibits outstanding catalytic performance, achieving NH_3 conversions of 76% at 500 °C and 95% at 550 °C with excellent stability. Through a combination of comprehensive characterization and density functional theory (DFT) calculations, we demonstrate that incorporated Sr species dynamically redistribute under reaction conditions, which is pivotal for fully leveraging their electron-donating capability. And Sr incorporation drives the generation of abundant oxygen vacancies and a strengthened metal–support interaction. These changes collectively optimize the electronic structure of the Co active centers, which in turn strengthens N–H bond activation and weakens the binding of reaction products, thereby accelerating the catalytic cycle. Our findings provide fundamental insights into support engineering *via* aliovalent doping, offering a strategic direction for developing high-performance, Co-based catalysts for NH_3 decomposition.

Experimental

Catalyst preparation

The Co/CeO_2 and $Co/Sr–CeO_2$ catalysts were prepared by a simple sol–gel method.[24] In a typical procedure for $Co/Sr–CeO_2$, $Co(NO_3)_3{\cdot}6H_2O$ (40 mmol) was first dissolved in 50 mL of deionized water, followed by the addition of 19.21 g of anhydrous citric acid and 5.59 mL of ethylene glycol. Subsequently, $Sr(NO_3)_2{\cdot}6H_2O$ (2 mmol) and $Ce(NO_3)_3{\cdot}6H_2O$ (8 mmol) were introduced into the solution. The mixture was heated at 100 °C to evaporate the water, and the resulting solid was dried and subsequently calcined at 300 °C for 3 h, followed by further calcination at 600 °C for 5 h. The final product was designated as $Co/Sr–CeO_2$. For the Co/CeO_2 catalyst, the same procedure was applied except that $Sr(NO_3)_2{\cdot}6H_2O$ was omitted and the amount of $Ce(NO_3)_3{\cdot}6H_2O$ was increased to 10 mmol.

Catalyst characterization

The X-ray diffraction (XRD) patterns were collected on a MiniFlex600 operating at 15 mA and 40 kV using Cu Kα (λ = 0.15406 nm) radiation. The scanning rate was 7° min^{-1} in the 2θ range of 10–80°. The morphology and microstructure of the catalysts were characterized by using a transmission electron microscope (TEM). High-angle annular dark-field STEM (HAADF-STEM) and EDS images were acquired using an FEI-Tecnai G2 F30 (USA) operated at 200 kV. To prepare the catalyst for TEM, a small amount of reduced catalyst was dispersed in 1 mL of ethanol and sonicated for 15 s. The resulting suspension was then deposited dropwise onto copper grids. The specific surface area and pore size distribution of the catalysts were analyzed *via* N_2 physisorption at 77 K using a Micromeritics ASAP 2020 analyzer. Prior to analysis, all samples were degassed under vacuum at 200 °C for 5 h. The corresponding surface area and pore size distribution were calculated using the Brunauer–Emmett–Teller (BET) and Barrett–Joyner–Halenda (BJH) methods, respectively. X-ray photoelectron spectroscopy (XPS) analysis of the reduced catalysts was performed on a Thermo Scientific K-ALPHA instrument with Al Kα radiation. All spectra were calibrated based on the standard C 1s binding energy of 284.8 eV. The EPR spin trapping experiments were performed on an EMX Plus measurement kit.

H_2 temperature-programmed reduction (H_2-TPR) experiments were carried out using a VDSORB-9i analyzer equipped with a thermal conductivity detector (TCD). Prior to analysis, approximately 100 mg of the catalyst was pretreated in high-purity Ar at 300 °C for 1 h and then cooled to room temperature. The reduction profile was subsequently recorded by heating the sample from 50 to 800 °C at a rate of 10 °C min^{-1} under a flowing gas mixture of 5% H_2/Ar.

The temperature-programmed desorption (TPD) profiles of NH_3, N_2, H_2, and CO_2 were obtained using a VDSORB-9i instrument. For each measurement, 100 mg of the reduced catalyst was pretreated at 300 °C for 1 h under a He flow (40 mL min^{-1}) and then cooled to room temperature. Subsequently, the sample was exposed to a flow (40 mL min^{-1}) of the respective probe gas (1% NH_3/Ar, N_2, 5% H_2/Ar or CO_2) for 1 h to achieve adsorption saturation. The system was then purged with He for 1 h to remove any gaseous or physisorbed species. Finally, the TPD signal was recorded by heating the sample from 50 to 800 °C at a linear rate of 10 °C min^{-1}.

Ammonia decomposition performance test

Catalytic activity for NH_3 decomposition was assessed using a fixed-bed reactor at atmospheric pressure. Typically, 100 mg of the sieved catalyst (20–40 mesh) was loaded into an 8 mm inner-diameter stainless-steel reactor, with a thermocouple placed on the outer wall of the stainless steel reactor to monitor the real-time temperature. Prior to reaction, the catalyst was heated to 400 °C at 5 °C min^{-1} under Ar and then reduced in a 20% H_2/Ar stream at 400 °C for 1 h. After reduction, the system was cooled to 350 °C under Ar. The reaction was initiated by switching the feed gas to pure NH_3 (50 mL min^{-1}). The temperature was raised stepwise from 350 to 600 °C in increments of 50 °C. At each temperature step, the catalyst was held for 30 min to reach steady state before the effluent gas was analyzed using an online gas chromatograph (GC9790II).

The NH_3 conversion, denoted as X_{NH_3}, was calculated using:

$$X_{NH_3} = \frac{[NH_3]_{inlet} - [NH_3]_{outlet}}{[NH_3]_{inlet}} \times 100\%$$

where $[NH_3]_{inlet}$ and $[NH_3]_{outlet}$ are the NH_3 concentrations measured at the reactor inlet and outlet, respectively.

The H_2 production rate (mmol g^{-1} min^{-1}) was calculated according to:

$$H_2 \text{ production rate} = \frac{3 \times v_{NH_3} \times X_{NH_3}}{2 \times 22.4 \times m_{cat}}$$

where v_{NH_3} refers to the NH_3 molar flow rate (mL min^{-1}) and m_{cat} is the catalyst mass (mg).

The activation energy (E_a) of the catalyst was determined from the Arrhenius plots:

$$k = A \exp\left(\frac{-E_a}{RT}\right)$$

where k represents the reaction rate constant, A is the frequency factor, R denotes the gas constant, and T refers to the absolute temperature.

Computational details

Spin-polarized density functional theory (DFT) calculations were performed using the Vienna *ab initio* simulation package (VASP) version 5.4.[25] The GGA-PBE functional was used for the exchange–correlation potential.[26] A plane-wave basis set with an energy cut-off of 400 eV was employed within the projector-augmented wave (PAW) framework.[27] The Brillouin zone was sampled using a 1 × 1 × 1 Monkhorst–Pack k-point mesh (refer to the k mesh validation in Fig. S13 and notes related). All atomic positions were fully relaxed until the Hellmann–Feynman forces on each atom were less than 0.02 eV $Å^{-1}$. The CeO_2 (111) surface was constructed using a three-layer O–Ce–O slab with a 15 Å vacuum region. The bottom layer was fixed, while the upper layers and all adsorbed species were fully relaxed. Sr doping was introduced by replacing one Ce atom with Sr in the slab, and oxygen vacancies were added to maintain charge neutrality. Furthermore, a Co nanoparticle was represented by six Co atoms placed on the CeO_2 catalyst surface. To accurately describe the strong electron correlation in the Ce 4f and Co 3d orbitals, a Hubbard U correction (DFT + U) was applied, with effective U values set to 4.5 eV for Ce 4f and 3.0 eV for Co 3d, consistent with previous studies.[28,29] Finally, the charge density and density of states (DOS) were analyzed using the VASPKIT code.[30]

The adsorption energy (ΔE_{ads}) between NH_3 and the reaction intermediate on the catalyst was evaluated as:

$$\Delta E_{ads} = E_{adsorbate/catalyst} - E_{catalyst} - E_{adsorbate}$$

where $E_{adsorbate/catalyst}$, $E_{catalyst}$, and $E_{adsorbate}$ represent the total energy of the adsorbed system, the energy of the optimized catalyst slab and the isolated adsorbate molecule in the gas phase, respectively.

The free energy (ΔG) for each elemental reaction step was obtained *via*:

$$\Delta G = \Delta E + \Delta E_{ZPE} - T\Delta S$$

where ΔE, ΔE_{ZPE} and ΔS represent the DFT-calculated adsorption energy, zero-point energy correction, and entropy change of the adsorption complex, respectively. T denotes the temperature (set to 500 °C in this study).

Results and discussion

Evaluation of NH_3 decomposition performance

A series of Co-based catalysts were synthesized *via* the sol–gel method. Co supported on CeO_2 (Co/CeO_2) can achieve 60% NH_3 conversion at 500 °C under a gas hourly space velocity (GHSV) of 30 000 mL g^{-1} h^{-1} (Fig. 1a). To further enhance the activity, various promoters (Sr, La, Ba, Y, Sm, Ca) were incorporated into the CeO_2 support. Among them, the alkaline-earth metal Sr exhibited the most pronounced promotional effect, yielding the highest NH_3 conversion (Fig. S1).

Subsequently, the Sr doping concentration was optimized. The NH_3 conversion followed a volcano-type trend with increasing Sr content, peaking at an optimal Sr : Ce molar ratio of 1 : 4 (Co/Sr_2–CeO_2; Fig. S2). The Co loading was also tuned, with catalytic activity reaching a maximum at a Co : (Sr + Ce) molar ratio of 4 : 1 (Fig. S3). This optimal ratio likely ensures a high density of accessible active sites while maintaining effective dispersion and a strong metal–support interaction. Furthermore, the reduction temperature in H_2 was found to have a negligible impact on the final catalytic performance within the tested range (Fig. S4). The comprehensively optimized Co/Sr–CeO_2 catalyst (Sr : Ce = 1 : 4, Co : (Sr + Ce) = 4 : 1, reduced at 400 °C) exhibited outstanding performance, achieving NH_3 conversions of approximately 76% at 500 °C and 95% at 550 °C, with a maximum hydrogen production rate reaching 32.4 mmol g^{-1} min^{-1} at a GHSV of 30 000 mL g^{-1} h^{-1} (Fig. 1a and b). Notably, the hydrogen production rate further increased to 387.2 mmol g^{-1} min^{-1} at 550 °C with a higher GHSV of 540 000 mL g^{-1} h^{-1} (Fig. S5). This performance is superior to most reported Co-based catalysts under comparable conditions[11,31–40] (Fig. 1c and Table S1). The apparent activation energy of the catalysts measured in the kinetic interval is shown in Fig. 1d, which is 80.03 kJ mol^{-1} for the Co/Sr–CeO_2 catalyst, much lower than those of Co/CeO_2 (105.74 kJ mol^{-1}), Co/SrO (96.90 kJ mol^{-1}) and Co (162.69 kJ mol^{-1}) catalysts. The catalytic performance and kinetic parameter indicated that the Sr doping enhanced the interactions between the components and accelerated the kinetic catalytic process of the NH_3 decomposition reaction.

To investigate the effect of GHSV on NH_3 conversion, the NH_3 decomposition performance of Co/Sr–CeO_2 was evaluated at varying temperatures and GHSV. As depicted in Fig. 1e and S6, NH_3 conversion at 600 °C remained >99% even at a high

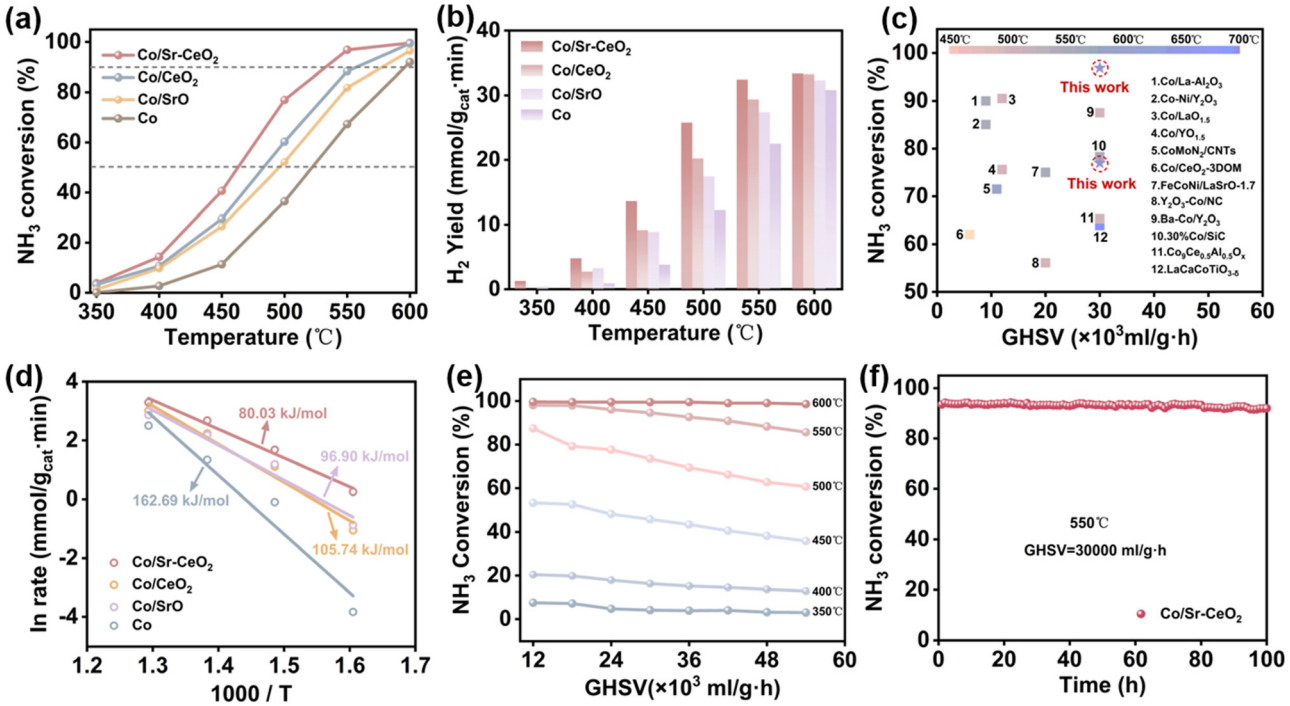

Fig. 1 (a) NH_3 decomposition conversion and (b) H_2 yield over different catalysts; (c) comparison of catalyst activity for NH_3 decomposition; (d) the apparent activation energy (E_a) for the prepared catalysts; (e) the effect of GHSV on the NH_3 conversion on the Co/Sr–CeO_2 catalyst at varying temperatures; (f) the stability test of NH_3 decomposition over the Co/Sr–CeO_2 catalyst at 550 °C and GHSV of 30 000 mL g^{-1} h^{-1}.

GHSV of 54 000 mL g^{-1} h^{-1}, attributable to the rapid reaction kinetics. However, the NH_3 conversion rate decreased with the increase of GHSV below 600 °C. This is because the higher flow rate reduces the contact time between NH_3 and the catalyst, leaving insufficient time for complete reaction before the gas exits.

The long-term stability of the Co/Sr–CeO_2 catalyst, a critical parameter for practical application, was assessed at 550 °C and a high GHSV of 30 000 mL g^{-1} h^{-1} for 100 h. Remarkably, the NH_3 conversion rate remained stable without noticeable decline throughout the entire testing period (Fig. 1f). This outstanding durability underscores the robust structural integrity of the catalyst, effectively resisting active site sintering or deactivation under the harsh reaction environment.

Catalyst structural characterization

To elucidate the structural influence of Sr doping and uncover the origin of the enhanced activity, X-ray diffraction (XRD) analysis was first conducted on the as-prepared catalysts. As shown in Fig. 2a, all the catalysts exhibited prominent diffraction peaks at 2θ = 19.0°, 31.2°, 36.8°, 44.8°, 59.4° and 65.0° that are well-indexed to the cubic spinel Co_3O_4 (PDF#00-0166). The introduction of CeO_2 and SrO leads to a gradual broadening and weakening of the Co_3O_4 peaks, indicating that the presence of these oxides effectively suppresses the growth of Co_3O_4 crystallites (Fig. 2b). Distinct diffraction patterns corresponding to CeO_2 and $SrO/SrCO_3$ are observed in the Co/CeO_2 and Co/SrO samples, respectively. In contrast, the XRD pattern of the optimized Co/Sr–CeO_2 catalyst exhibits significant attenuation and broadening for both the Co_3O_4 and CeO_2-related peaks. Importantly, the CeO_2 diffraction peaks shift toward lower angles, indicating an expansion of its lattice (Fig. 2c). These observations strongly suggest the successful incorporation of some Sr^{2+} into the CeO_2 lattice to form a Sr–CeO_2 solid solution. The substitution of smaller Ce^{4+} ions with larger Sr^{2+} ions induces substantial lattice distortion and tensile strain, which not only expands the lattice but also reduces the overall crystallinity of the CeO_2 framework. Such structural modification is highly conducive to the generation of abundant oxygen vacancies. The observed attenuated and broadened Co_3O_4 diffraction peaks in Co/Sr–CeO_2 signal a significantly enhanced metal–support interaction (MSI). This is facilitated by the modified structure of the Sr–CeO_2 support, which provides strong anchoring sites for Co nanoparticles, resulting in improved dispersion and superior resistance against sintering. The average crystallite size of the Co_3O_4 phase was further estimated using the Scherrer equation. The Co_3O_4 crystallites in Co/Sr–CeO_2 are notably smaller (~13.87 nm) than those in the Co/CeO_2 (~26.46 nm) and pure Co nanoparticles (~39.07 nm), providing direct evidence that Sr doping effectively stabilizes Co species against particle growth during synthesis (Table S2). Following H_2 reduction, the Co_3O_4 phase in all catalysts was completely converted to metallic Co nanoparticles (Fig. S7). In the spent Co/Sr–CeO_2 catalyst, the diffraction features associated with Sr species diminished significantly, suggesting that the NH_3

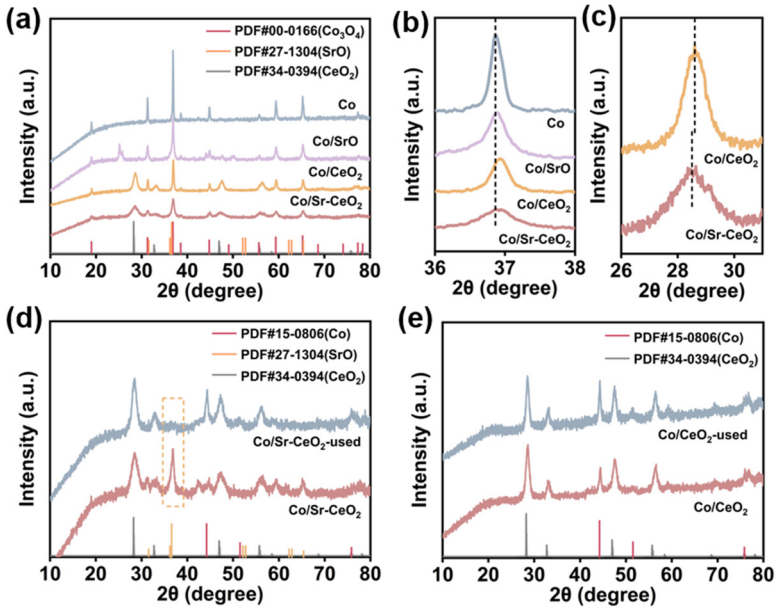

Fig. 2 (a) XRD patterns and (b and c) enlarged XRD patterns of Co/Sr–CeO_2, Co/CeO_2, Co/SrO and Co catalysts; (d) XRD patterns of Co/Sr–CeO_2 after H_2 reduction and the Co/Sr–CeO_2-used catalyst; (e) XRD patterns of Co/CeO_2 after H_2 reduction and the Co/CeO_2-used catalyst.

decomposition process promotes further redistribution and dispersion of Sr (Fig. 2d). Moreover, the spent Co/CeO_2 catalyst exhibits metallic Co diffraction peaks that are more intense and sharper than those of the spent Co/Sr–CeO_2 catalyst. This indicates a larger average crystalline size of the metallic Co nanoparticles in Co/CeO_2, further demonstrating that Sr doping effectively enhances the dispersion and inhibits the sintering of Co nanoparticles during the reaction (Fig. 2d and e).

To further elucidate the interaction between Co and the Sr doped CeO_2 support, transmission electron microscopy (TEM) analysis was performed on the Co/Sr–CeO_2 catalyst before and after the NH_3 decomposition reaction (Fig. 3). Comparative TEM images show that the catalyst maintained its structural integrity without significant particle sintering or morphological collapse during the reaction process (Fig. 3a and e). High-resolution TEM (HRTEM) images of the fresh catalyst reveal distinct lattice fringes with spacings of 0.31 nm and 0.21 nm, corresponding to the (111) planes of CeO_2 and metallic Co, respectively[11,39] (Fig. 3b and c). Notably, these characteristic lattice fringes remain clearly visible in the spent catalyst, confirming that the crystalline phases of both Co and CeO_2 are well preserved and possess good thermal and structural stability under operating conditions (Fig. 3f and g). Energy-dispersive X-ray spectroscopy (EDS) mapping was employed to further investigate the elemental distribution and its evolution. In the fresh Co/Sr–CeO_2 catalyst, Sr species are present as localized aggregates (Fig. 3d). Notably, after the reaction, Sr exhibits a significantly more homogeneous distribution throughout the catalyst architecture (Fig. 3h). This redistribution, promoted by the high-temperature reducing atmosphere during NH_3 decomposition, aligns well with the XRD observations. Importantly, a comparative analysis of the Co distribution reveals that Co nanoparticles in the Co/Sr–CeO_2 catalyst remain notably more dispersed than those in the Co/CeO_2 counterpart, where severe Co aggregation is observed (Fig. 3d and S8). This contrast provides direct spatial evidence that Sr doping into the CeO_2 framework effectively stabilizes and anchors Co nanoparticles, thereby inhibiting their sintering during both the synthesis and catalytic process. Furthermore, the resulting increase in the number of well-dispersed, accessible Co active sites is likely a key factor contributing to the significantly enhanced performance of the Co/Sr–CeO_2 catalyst.

The textural properties of the catalysts were analysed by N_2 physisorption (Fig. S9 and Table S3). Relative to the low surface area Co reference, the introduction of a CeO_2 support in Co/CeO_2 significantly increased both the specific surface area and pore volume, which is attributed to the inherently higher surface area of CeO_2 and facilitates the dispersion of active Co species. Notably, Sr doping in Co/Sr–CeO_2 induced a distinct reduction in the surface area and pore volume compared to Co/CeO_2, accompanied by further pore narrowing. This textural change can be explained by the presence of aggregated SrO_x/$SrCO_3$ clusters in the fresh catalyst, which likely partially block the pore channels and cover surface sites. These results initially suggest that the higher surface area of Co/CeO_2 contributes to its improved activity over bare Co by providing more accessible sites. However, Co/Sr–CeO_2 exhibits the optimal performance despite having a relatively lower surface area. This clearly indicates that the chemical promotion effect of Sr doping outweighs purely textural advantages. Therefore, the exceptional activity of Co/Sr–CeO_2 is primarily governed by Sr-induced synergistic effects, such as enhanced oxygen vacancy concentration and optimized metal–support interactions, rather than by the specific surface area alone.

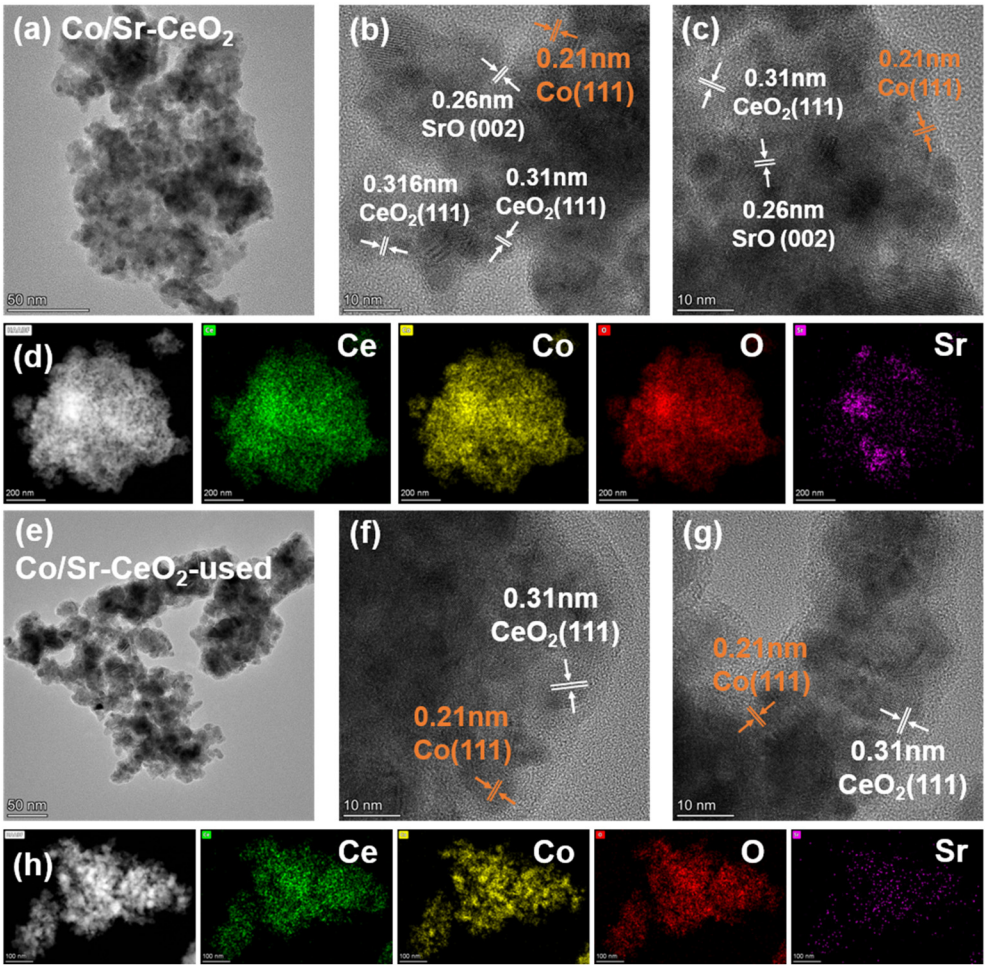

Fig. 3 (a) TEM image and (b and c) HR-TEM images with marked lattice fringes of the Co/Sr–CeO_2 catalyst. (d) The corresponding elemental mappings of the Co/Sr–CeO_2 catalyst. (e) TEM image and (f and g) HR-TEM images with marked lattice fringes of the used Co/Sr–CeO_2 catalyst. (h) The corresponding elemental mappings of the used Co/Sr–CeO_2 catalyst.

X-ray photoelectron spectroscopy (XPS) was conducted on the fresh and spent catalysts to elucidate the electronic structure modifications induced by Sr doping (Fig. 4). The Co 2p spectra of all catalysts exhibit characteristic peaks corresponding to Co^0, Co^{2+}, and Co^{3+} species[41] (Fig. 4a). Notably, a distinct shift toward lower binding energy is observed for Co/Sr–CeO_2 compared to both Co/CeO_2 and pure Co, indicating an increased electron density on the Co active sites. This electronic enrichment originates from charge transfer from the Sr-modified CeO_2 support to the Co nanoparticles, which optimizes the electronic state of Co for catalytic activation. The Sr 3d spectra offer insight into the chemical state and evolution of Sr. The Sr $3d_{5/2}$ peak at 133.23 eV could be assigned to strontium carbonate species. In Co/SrO, the pronounced intensity of this higher-binding-energy doublet aligns with its high surface Sr content and is consistent with the tendency of SrO to adsorb atmospheric CO_2 (ref. 42) (Fig. 4b and S10). In contrast, the spent Co/Sr–CeO_2 catalyst shows a noticeable increase in the lower-binding-energy component of the Sr 3d spectrum, suggesting an elevated electron density around Sr after the reaction (Fig. 4c). Combined with post-reaction XRD and TEM evidence of improved Sr dispersion, this indicates that initially aggregated SrO_x species decompose and redistribute under reaction conditions, likely to incorporate into the CeO_2 lattice or reside at the Co–CeO_2 surface. Complementary evidence from the Ce 3d spectra further elucidates the role of Sr. The Ce 3d spectrum exhibited a mixed valence state of Ce^{4+}/Ce^{3+} (ref. 15 and 20) (Fig. 4d). Deconvolution shows a significantly higher proportion of Ce^{3+} species in Co/Sr–CeO_2 than in Co/CeO_2 (Table S4). Since Ce^{3+} is intrinsically associated with oxygen vacancies, this confirms that Sr doping successfully increases the oxygen vacancy concentration within the CeO_2 lattice.[43,44] Notably, the Ce^{3+} signal is further intensified in the spent Co/Sr–CeO_2 catalyst, suggesting the continuous generation of oxygen vacancies during the reaction, likely promoted by the redistribution of Sr species. (Fig. S11 and Table S4). The concentration of oxygen vacancies induced by Sr doping was further quantified by electron paramagnetic resonance (EPR). As shown in Fig. 4e, the EPR signal intensity at g = 2.003 corresponding to oxygen vacancies is significantly stronger for spent Co/Sr–CeO_2 than that for the Co/CeO_2 catalyst.[45,46] The excellent agreement between the enhanced

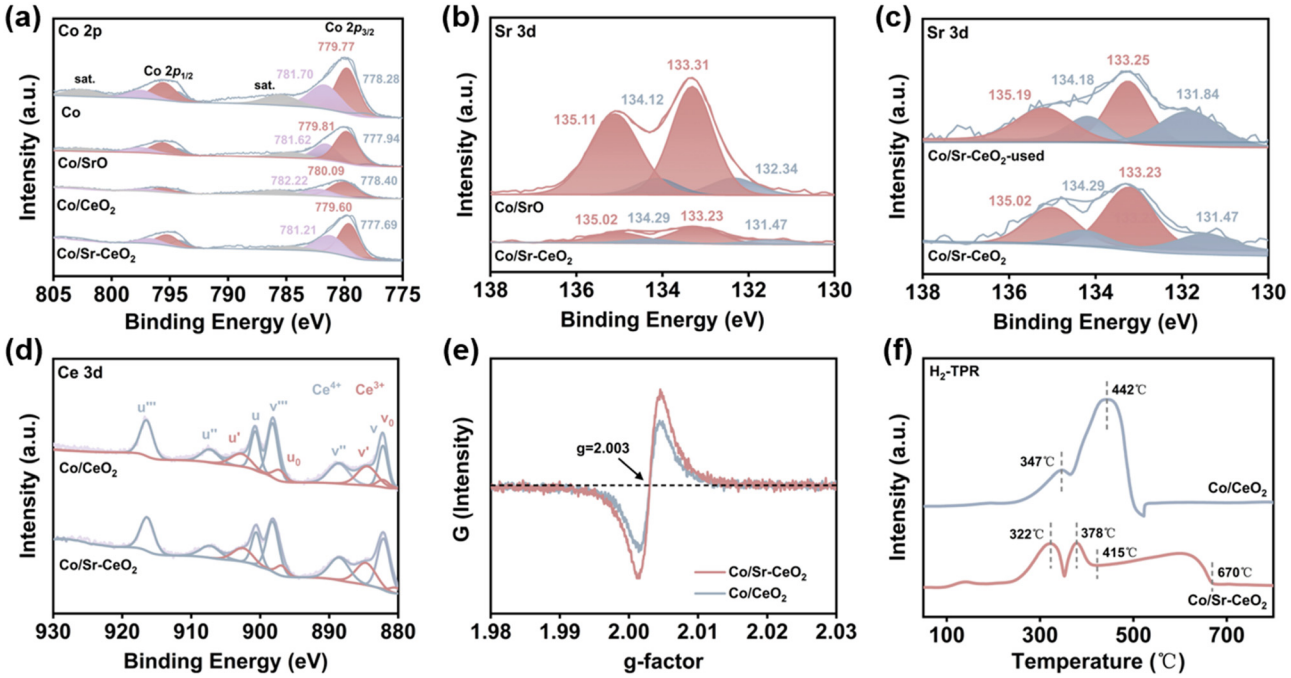

Fig. 4 High-resolution XPS spectra of the prepared catalysts for (a) Co 2p and (b) Sr 3d. (c) High-resolution Sr 3d XPS spectra of the used Co/Sr–CeO_2 catalysts. (d) High-resolution Ce 3d XPS spectra of Co/Sr–CeO_2 and Co/CeO_2 catalysts. (e) EPR and (f) H_2-TPR spectra of Co/Sr–CeO_2 and Co/CeO_2 catalysts.

Ce^{3+} concentration and the intensified EPR signal solidly confirms that Sr doping successfully engineers a CeO_2 support rich in oxygen vacancies. Collectively, the incorporation and dynamic redistribution of Sr modulate the local electronic structure of the catalyst, promotes the formation of surface oxygen vacancies, and optimizes the Co–support interaction. This synergistic effect is the key reason why Co/Sr–CeO_2 outperforms Co/CeO_2 in NH_3 decomposition, despite the latter having a larger specific surface area.

This Sr-induced defective structure critically alters the reducibility and metal–support interaction, as revealed by H_2-TPR (Fig. 4f). The observed reduction features correspond to the stepwise reduction of Co^{3+} to Co^{2+} and subsequently to metallic Co^0.[39,41] Notably, for the Co/Sr–CeO_2 catalyst, the primary reduction peaks shift toward lower temperatures. Specifically, the main Co oxide reduction splits into two peaks at 322 °C and 378 °C. Concurrently, a broad reduction peak emerges at higher temperatures, spanning from approximately 415 °C to 670 °C, attributed to the reduction of strongly interfacial-coupled Co nanoparticles and the Sr-modified CeO_2 support itself.[47–49] This pronounced downward shift in reduction temperatures clearly indicates that Sr doping significantly enhances the reducibility of the catalyst.[42] The promotion effect is ascribed to the Sr-induced oxygen vacancies, which facilitate hydrogen activation and electron transfer, thereby lowering the energy barrier for the reduction of both Co and Ce species. Furthermore, the increased contribution of the high-temperature reduction feature provides direct evidence for a stronger metal–support interaction in Co/Sr–CeO_2. This enhanced interaction promotes electron transfer across the interface and effectively stabilizes the Co nanoparticles against sintering, which is consistent with the catalyst's excellent stability during NH_3 decomposition.

Mechanism analysis for NH_3 decomposition

To gain mechanistic insights into the superior activity of Co/Sr–CeO_2, we systematically investigated the surface properties of the catalysts and their adsorption and desorption ability for key reaction species using temperature-programmed desorption (TPD). CO_2-TPD was first employed to probe the basic characteristics and evaluate the promotional effect of the Sr doping for thermal catalytic NH_3 decomposition.[50] As shown in Fig. 5a, Co/CeO_2 displays two desorption peaks at 89 °C and 376 °C, corresponding to weak and moderately strong basic sites, respectively. In contrast, Co/Sr–CeO_2 exhibits an additional peak at 211 °C, alongside a slight shift of the high-temperature peak to 382 °C with markedly enhanced intensity. These modifications reveal that Sr doping elevates the density of basic sites, particularly those of moderate strength. This enhanced basicity favors the cleavage of N–H bonds and N_2 desorption, *via* direct H abstraction and indirect electronic modification of Co active sites.[20,36]

The acidic properties and reactant adsorption strength were analyzed using NH_3-TPD.[41,51] The results in Fig. 5b show that Co/CeO_2 exhibits two peaks at 85 °C and 484 °C, corresponding to weak and strong acidic sites, respectively. For Co/Sr–CeO_2, the weak-acid peak at 92 °C is intensified, while the high-temperature peak shifts downward to 435 °C.

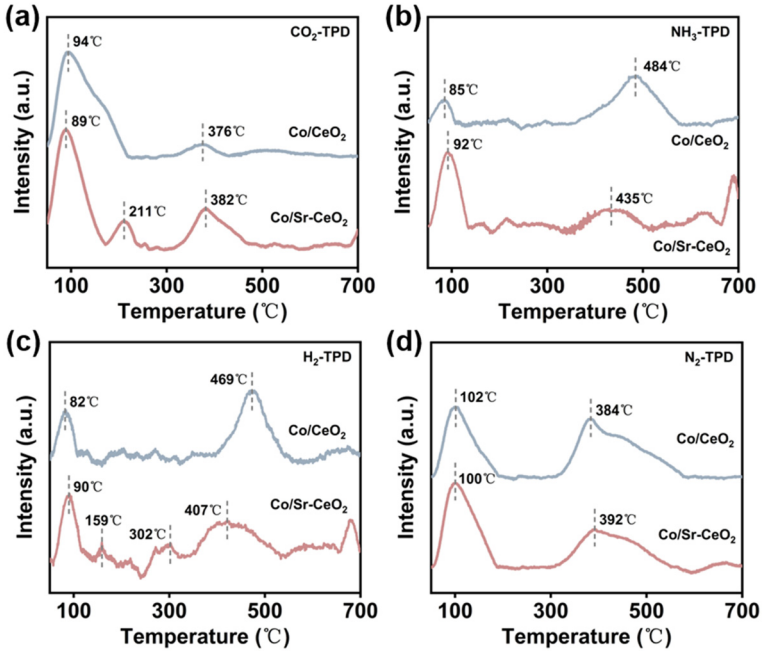

Fig. 5 Temperature dependence of gas species adsorption on Co/CeO_2 and $Co/Sr–CeO_2$ catalysts. (a) CO_2-TPD, (b) NH_3-TPD, (c) H_2-TPD and (d) N_2-TPD profiles of $Co/Sr–CeO_2$ and Co/CeO_2 catalysts.

This suggests that Sr doping reduces both the density and strength of strong acidic sites. Such a moderate NH_3 binding facilitates the desorption of reaction products and thereby promotes the forward reaction. H_2-TPD profiles display a similar trend. Co/CeO_2 shows desorption peaks at 82 °C (weakly adsorbed H) and 469 °C (strongly adsorbed H) (Fig. 5c). $Co/Sr–CeO_2$ displays additional features at 159 °C and 302 °C, and the high-temperature peak shifts to a lower temperature of 407 °C. These changes imply that Sr doping weakens the binding strength of strongly adsorbed hydrogen, which not only facilitates H_2 desorption but also helps prevent active-site blocking by strongly bound H species. Finally, N_2-TPD further corroborates this optimization (Fig. 5d). Compared to Co/CeO_2 (peaks at 102 °C and 384 °C), $Co/Sr–CeO_2$ shows an intensified low-temperature peak at 100 °C. Although its high-temperature peak shifts slightly to 392 °C, the quantity of strongly bound N species is markedly reduced, leading to overall easier desorption.

In summary, the collective TPD evidence demonstrates that Sr doping induces a concerted modulation of the catalyst's surface properties. It enhances surface basicity while attenuating strong acidity, thereby promoting both NH_3 activation and product desorption. Concurrently, it optimizes the desorption behavior of hydrogen and nitrogen species, preventing active-site blockage and contributing to sustained catalytic durability. These coordinated modifications collectively underpin the superior NH_3 decomposition performance of $Co/Sr–CeO_2$.

DFT calculations

To unravel the origin of the superior NH_3 decomposition activity of $Co/Sr–CeO_2$ at the atomic scale, density functional theory (DFT) calculations were performed. The computational models focused on Co clusters supported on the pristine CeO_2 (111) and Sr-doped CeO_2 (111) surfaces to mimic the local interfacial structure (Fig. S12).

The DFT results indicate that Sr doping significantly lowers the formation energy of oxygen vacancies in the CeO_2 support, providing a theoretical foundation for the higher oxygen vacancy concentration confirmed experimentally by Ce 3d XPS and EPR (Fig. 6a and S13). Differential charge density analysis reveals enhanced electron redistribution between the Co nanoparticles and the $Sr–CeO_2$ support, indicating a stronger metal–support interaction (Fig. 6b). Consistent with this, Bader charge analysis also reveals that the Co nanoparticle in the $Co/Sr–CeO_2$ catalyst carries a higher positive charge compared to that in Co/CeO_2. Furthermore, the d-band center of the $Co/Sr–CeO_2$ catalyst is shifted closer to the Fermi level, which reduces the energy gap between the Co 3d orbitals and the antibonding orbitals of the NH_3 molecule, thereby enhancing the activation capability of the Co active sites toward NH_3 (Fig. 6c and d).

Regarding NH_3 adsorption, both $Co/Sr–CeO_2$ and Co/CeO_2 exhibit comparable adsorption strengths (Fig. 6e). However, after adsorption, the N–H bond length elongates from 1.024 Å in the free NH_3 molecule to 1.029 Å on $Co/Sr–CeO_2$ and 1.027 Å on Co/CeO_2, indicating a stronger activation ability of the Sr-doped catalyst. Crystal orbital Hamilton population (COHP) analysis further supports this observation (Fig. 6f). The appearance of negative peaks below the Fermi level in the COHP curves for the N–H bonds confirms the population of antibonding orbitals upon NH_3 adsorption on both catalysts, leading to bond activation. This effect is quantitatively confirmed by the integrated COHP (ICOHP);

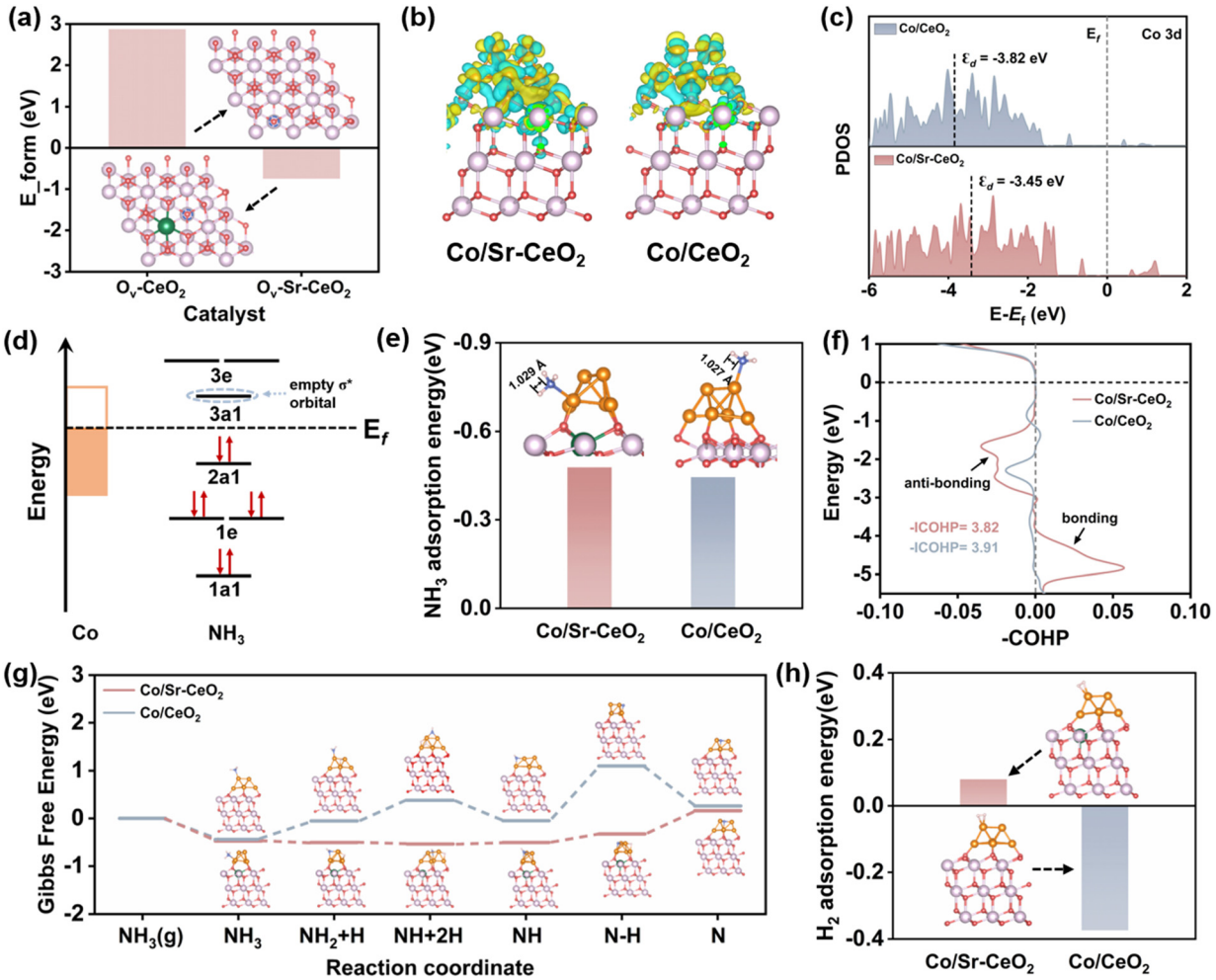

Fig. 6 (a) The formation energy of oxygen vacancies (O_v) over CeO_2 and Sr–CeO_2 catalysts. Blue circle represents O_v. (b) Charge density differences of Co/Sr–CeO_2 and Co/CeO_2 catalysts; yellow isosurfaces denote where electron density increases and blue isosurfaces denote where electron density decreases. (c) Projected density of states (PDOS) of Co 3d orbitals and d-band centers of the Co/Sr–CeO_2 and Co/CeO_2 catalysts. (d) Schematic diagram of electron transfer in NH_3 adsorption on the Co site. (e) The adsorption energy and adsorption structure of NH_3 on the catalyst surface. (f) The COHP analysis of the N–H bond upon NH_3 adsorption on the Co/Sr–CeO_2 and Co/CeO_2 catalysts. (g) Free energy profiles for the stepwise dehydrogenation of NH_x on the Co/Sr–CeO_2 and Co/CeO_2 catalysts (temperature was set to 500 °C). (h) The adsorption energy and adsorption structure of H_2 on the catalysts surface.

the smaller ICOHP value for Co/Sr–CeO_2 signifies more pronounced N–H bond weakening compared to Co/CeO_2, thereby facilitating N–H bond cleavage.

The calculated reaction energies for the stepwise N–H bond cleavage during NH_3 decomposition are summarized in Fig. 6g. All key intermediates (NH_2, NH, N*) on the Co/Sr–CeO_2 surface exhibited significantly lower energies compared to those on Co/CeO_2. This indicates that the unique electronic structure of Co/Sr–CeO_2 enhances the adsorption of dehydrogenation intermediates, thereby facilitating the reaction process. Moreover, Co/Sr–CeO_2 shows a relatively weak adsorption for the reaction product H_2, in agreement with the H_2-TPD results (Fig. 6h and S14). Together, these features effectively prevent excessive accumulation of surface H* and N* species.

In summary, DFT calculations reveal that Sr doping fundamentally modulates the electronic structure at the Co–CeO_2 system. The optimized charge redistribution and a lowered oxygen vacancy formation energy simultaneously enhance N–H bond activation and alleviate excessive accumulation of poisoning H* and N* species. These atomic-scale insights provide a direct theoretical basis for the superior NH_3 decomposition performance of Co/Sr–CeO_2, aligning perfectly with the trends observed in experimental characterization.

Conclusions

In summary, this study demonstrates that Sr doping in the Co/CeO_2 catalyst serves as a powerful strategy to engineer a high-performance Co-based catalyst for efficient NH_3 decomposition. The incorporation and subsequent dynamic redistribution of Sr under reaction conditions enhance the surface basicity of Co/Sr–CeO_2 and promote the formation of abundant oxygen vacancies. This optimized structure fosters

a strong metal–support interaction, which effectively stabilizes and disperses Co nanoparticles, prevents their sintering and aggregation at high temperatures, and thereby ensures the structural and catalytic activity stability of the catalyst. Moreover, these synergistic modifications induce profound optimization of the electronic structure. The resulting electronic environment of Co/Sr–CeO_2 strengthens the activation of NH_3 while weakening the binding strength of products, especially H_2. This dual effect mitigates active site poisoning and accelerates the catalytic cycle. Therefore, tailoring the electronic structure of catalyst supports through alkaline earth metal doping presents a potent and rational strategy for the design of advanced catalysts.

Conflicts of interest

There are no conflicts to declare.

Data availability

Data will be provided and available upon request. Supplementary information (SI): additional experimental data to support the findings presented in the main text. This includes catalytic performance screening of various promoters and optimization of reaction conditions. Detailed structural characterization of the catalysts is presented, including X-ray diffraction (XRD) patterns, transmission electron microscopy (TEM) images, N_2 physisorption isotherms and textural properties, and X-ray photoelectron spectroscopy (XPS) analyses. And supplementary DFT computational details and results are also included. See DOI: https://doi.org/10.1039/d6cy00086j.

Acknowledgements

This work was supported by the Sichuan Science and Technology Program (2026YFHZ0052) and the Natural Science Foundation of Sichuan Province (2025ZNSFSC0896).

References

1 S. Mukherjee, S. V. Devaguptapu, A. Sviripa, C. R. F. Lund and G. Wu, *Appl. Catal., B*, 2018, **226**, 162–181.
2 S. Mateti, L. Saranya, G. Sathikumar, Q. Cai, Y. Yao and Y. I. Chen, *Nanotechnology*, 2022, **33**, 222001.
3 I. Lucentini, X. Garcia, X. Vendrell and J. Llorca, *Ind. Eng. Chem. Res.*, 2021, **60**, 18560–18611.
4 S. Sun, Q. Jiang, D. Zhao, T. Cao, H. Sha, C. Zhang, H. Song and Z. Da, *Renewable Sustainable Energy Rev.*, 2022, **169**, 112918.
5 K. E. Lamb, M. D. Dolan and D. F. Kennedy, *Int. J. Hydrogen Energy*, 2019, **44**, 3580–3593.
6 J. E. Lee, J. Lee, H. Jeong, Y.-K. Park and B.-S. Kim, *Chem. Eng. J.*, 2023, **475**, 146108.
7 T. Han, L. Wei, S. Xie, Y. Liu, H. Dai and J. Deng, *Ind. Chem. Mater.*, 2025, **3**, 311–331.
8 Z. Yang, Z. Shui, M. Zhao, Z. Wei, F. Zhang, X. Duan, B. Niu, B. Li, G. Jiang and Z. Hao, *ACS Catal.*, 2025, **15**, 6255–6265.
9 W. U. Khan, H. S. Alasiri, S. A. Ali and M. M. Hossain, *Chem. Rec.*, 2022, **22**, e202200030.
10 B. S. Solanki, H. Lim, S. J. Yoon, H. C. Ham, H. S. Park, H. E. Lee and S. H. Lee, *Renewable Sustainable Energy Rev.*, 2025, **207**, 114974.
11 Y. Zhu, H. Pan, Q. Li, X. Huang, W. Xi, H. Tang, W. Tu, S. Wang, H. Tang and H. Zhang, *Adv. Sci.*, 2024, **11**, 2406659.
12 P. Zhou, G. Hai, G. Zhao, R. Li, X. Huang, Y. Lu and G. Wang, *Appl. Catal., B*, 2023, **325**, 122364.
13 X. Huang, K. Zhang, B. Peng, G. Wang, M. Muhler and F. Wang, *ACS Catal.*, 2021, **11**, 9618–9678.
14 T. Montini, M. Melchionna, M. Monai and P. Fornasiero, *Chem. Rev.*, 2016, **116**, 5987–6041.
15 L.-Y. Yan, X.-P. Fu, W.-W. Wang and C.-J. Jia, *Appl. Catal., B*, 2025, **378**, 125538.
16 X.-P. Fu, C.-P. Wu, W.-W. Wang, Z. Jin, J.-C. Liu, C. Ma and C.-J. Jia, *Nat. Commun.*, 2023, **14**, 6851.
17 D. Yu, L. Wang, C. Zhang, C. Peng, X. Yu, X. Fan, B. Liu, K. Li, Z. Li, Y. Wei, J. Liu and Z. Zhao, *ACS Catal.*, 2022, **12**, 15056–15075.
18 Z. Zhang, M. Yu, M. Shen, W. Li and G. Shen, *Mol. Catal.*, 2025, **578**, 115016.
19 N. Morlanés, S. Sayas, G. Shterk, S. P. Katikaneni, A. Harale, B. Solami and J. Gascon, *Catal. Sci. Technol.*, 2021, **11**, 3014–3024.
20 H. Tabassum, S. Mukherjee, J. Chen, D. Holiharimanana, S. Karakalos, X. Yang, S. Hwang, T. Zhang, B. Lu, M. Chen, Z. Tang, E. A. Kyriakidou, Q. Ge and G. Wu, *Energy Environ. Sci.*, 2022, **15**, 4190–4200.
21 H. Liu, J. Liang, J. Li, Y. Du, H. Chen, C. Du, L. Wang, Y. Li, Y. Huang and D. Chen, *Energy Fuels*, 2024, **38**, 13255–13263.
22 S. Sayas, N. Morlanés, S. P. Katikaneni, A. Harale, B. Solami and J. Gascon, *Catal. Sci. Technol.*, 2020, **10**, 5027–5035.
23 K. Liu, X. Xu, J. Xu, X. Fang, L. Liu and X. Wang, *J. CO2 Util.*, 2020, **38**, 113–124.
24 W. Ma, J. Morales-Vidal, J. Tian, M.-T. Liu, S. Jin, W. Ren, J. Taubmann, C. Chatzichristodoulou, J. Luterbacher, H. M. Chen, N. López and X. Hu, *Nature*, 2025, **641**, 1156–1161.
25 J. Hafner, *J. Comput. Chem.*, 2008, **29**, 2044–2078.
26 J. P. Perdew, K. Burke and M. Ernzerhof, *Phys. Rev. Lett.*, 1996, **77**, 3865–3868.
27 P. E. Blöchl, *Phys. Rev. B: Condens. Matter Mater. Phys.*, 1994, **50**, 17953–17979.
28 J. Zhang, X. Gong and G. Lu, *Chin. J. Catal.*, 2014, **35**, 1305–1317.
29 Lalmuanchhana, B. Lalroliana, R. C. Tiwari, Lalhriatzuala and R. Madaka, *Appl. Surf. Sci.*, 2022, **604**, 154570.
30 V. Wang, N. Xu, J.-C. Liu, G. Tang and W.-T. Geng, *Comput. Phys. Commun.*, 2021, **267**, 108033.
31 W. Wang, Y. Fu, W. Wang, M. Xiang, G. Chen, Y. Su and J. Duan, *Ceram. Int.*, 2024, **50**, 36604–36614.
32 H. Li, L. Guo, J. Qu, X. Fang, Y. Fu, J. Duan, W. Wang and C. Li, *Int. J. Hydrogen Energy*, 2023, **48**, 8985–8996.
33 H. Mizoguchi, S. Luo, M. Sasase, M. Kitano and H. Hosono, *J. Phys. Chem. Lett.*, 2025, **16**, 796–801.
34 Z. Zhao, H. Zou and W. Lin, *J. Rare Earths*, 2013, **31**, 247–250.

35 C. Huang, Y. Yu, X. Tang, Z. Liu, J. Zhang, C. Ye, Y. Ye and R. Zhang, *Appl. Surf. Sci.*, 2020, **532**, 147335.
36 Y. Li, K. Wang, Z. Wang, X. Wang, X. Chu, R. Zhang, S. Song, H. Zhang and X. Wang, *Adv. Energy Mater.*, 2025, 2405296–2405303.
37 K. Xu, Y.-Y. Zhang, W.-W. Wang, M. Peng, C. Ma, Y.-W. Zhang, C.-J. Jia, D. Ma and C.-H. Yan, *Angew. Chem.*, 2025, **64**, e202416195.
38 R. Xu, F. Yin, J. Zhang, G. Li, G. Kofie, Y. Tan and B. Chen, *Catal. Today*, 2024, **437**, 114774.
39 X.-C. Li, T.-T. Huang, Y. Hu, X. Li, Y.-F. Liu, H. Dong, C.-J. Jia, G.-S. Li and Y.-W. Zhang, *Appl. Catal., B*, 2025, **366**, 125020.
40 H. Jeong, Y. H. Kim, W. Jang, Y. Ji, J.-E. Hong and J. Myung, *Solid State Ionics*, 2024, **416**, 116679.
41 X. Han, M. Hu, J. Yu, X. Xu, P. Jing, B. Liu, R. Gao and J. Zhang, *Appl. Catal., B*, 2023, **328**, 122534.
42 X. Guo, J.-H. Wang, Q. Zhang, T.-Z. Li, H. Dong, C.-J. Jia, C. Li and Y.-W. Zhang, *Appl. Catal., B*, 2024, **348**, 123844.
43 Z. Chen, B. Jiang, Z. Lu, J. Huang, J. Shi and M. Liu, *Small*, 2025, 2500830.
44 C. Song, Q. Zhan, F. Liu, C. Wang, H. Li, X. Wang, X. Guo, Y. Cheng, W. Sun, L. Wang, J. Qian and B. Pan, *Angew. Chem., Int. Ed.*, 2022, **61**, e202200406.
45 F. Huang, X. Chen, H. Sun, Q. Zeng, J. Ma, D. Wei, J. Zhu, Z. Chen, T. Liang, X. Yin, X. Liu, J. Xu and H. He, *Angew. Chem.*, 2025, **64**, e202415642.
46 M. Wang, N. Shang, W. Gao, X. Cheng, S. Gao and C. Wang, *Fuel*, 2023, **354**, 129433.
47 X. Liao, Y. Zhang, J. Guo, L. Zhao, M. Hill, Z. Jiang and Y. Zhao, *Catalysts*, 2017, **7**, 272–287.
48 M. R. Ahasan, Y. Wang and R. Wang, *Mol. Catal.*, 2022, **518**, 112085.
49 H. Zhao, X.-P. Fu, W.-W. Wang, J.-C. Liu and C.-J. Jia, *Appl. Catal., B*, 2026, **385**, 126345.
50 R. Chen, H. Pan, Z. Meng, H. Tang, Q. Li, T. Tian, X. Huang, Z. Zhan and H. Tang, *Adv. Compos. Hybrid Mater.*, 2025, **8**, 164.
51 W. Zhang, W. Zhou, Y. Li, J. Ren and Z. Wang, *Appl. Catal., B*, 2023, **330**, 122644.